

Language-Enhanced Generative Modeling for PET Synthesis from MRI and Blood Biomarkers

Zhengjie Zhang^{a,1}, Xiaoxie Mao^{b,c,1}, Qihao Guo^d, Shaoting Zhang^a, Qi Huang^c, Mu Zhou^e, Fang Xie^{c,**}, Mianxin Liu^{a,f,*}

^aShanghai Artificial Intelligence Laboratory, Shanghai, 200082, China

^bSchool of Medicine, Xiamen University, Xiamen, Fujian, China

^cDepartment of Nuclear Medicine & PET Center, Huashan Hospital, Fudan University, Shanghai, China

^dDepartment of Gerontology, Shanghai Jiao Tong University Affiliated Sixth People's Hospital, Shanghai, China

^eDepartment of Computer Science, Rutgers University, New Brunswick, New Jersey, United States

^fShenzhen Institutes of Advanced Technology, Chinese Academy of Sciences, Shenzhen, China

Abstract

Background: Alzheimer's disease (AD) diagnosis heavily relies on amyloid-beta positron emission tomography (A β -PET), which is limited by its high cost and limited accessibility. This study explores whether A β -PET spatial patterns can be predicted from blood-based biomarkers (BBMs) and MRI scans.

Methods: We collected A β -PET images, T1-weighted MRI scans, and BBMs from 566 participants. A language-enhanced generative model, driven by a large language model (LLM) and multimodal information fusion, was developed to synthesize PET images. Synthesized images were evaluated for image quality, diagnostic consistency, and clinical applicability within a fully automated diagnostic pipeline.

Findings: The synthetic PET images closely resemble real PET scans in both structural details (SSIM = 0.920 ± 0.003) and regional patterns (Pear-

*Corresponding author. Email: liumianxin@pjlab.org.cn (M. Liu)

**Corresponding author. Email: fangxie@fudan.edu.cn (F. Xie)

Corresponding author. Email: muzhou1@gmail.com (M. Zhou)

Corresponding author. Email: hq_1124@163.com (Q. Huang)

¹These authors contributed equally to this work.

son’s $R = 0.955 \pm 0.007$). Diagnostic outcomes using synthetic PET show high agreement with real PET-based diagnoses (accuracy = 0.80). Using synthetic PET, we developed a fully automatic AD diagnostic pipeline integrating PET synthesis and classification. The synthetic PET-based model (AUC = 0.78) outperforms T1-based (AUC = 0.68) and BBM-based (AUC = 0.73) models, while combining synthetic PET and BBMs further improved performance (AUC = 0.79). Ablation analysis supports the advantages of LLM integration and prompt engineering.

Interpretation: Our language-enhanced generative model demonstrates strong capability in synthesizing realistic PET images, enhancing the utility of MRI and BBMs for $A\beta$ spatial pattern assessment and improving the diagnostic workflow for Alzheimer’s disease.

Keywords: Blood-based Biomarkers, PET Synthesis, Large Language Model, Multimodal, Generative Model

Research in Context

Evidence before this study

Alzheimer’s disease (AD) is a neurodegenerative disorder causing dementia in more than 55 million people globally, over 60% of whom live in low- and middle-income countries. The current gold standard for AD early diagnosis requires amyloid-beta positron emission tomography ($A\beta$ -PET), which is limited by its high cost and low accessibility in developing regions. Assessing PET with low cost and high accessibility is essential for large-scale AD screening. Existing studies have shown that magnetic resonance imaging (MRI) and blood-based biomarkers (BBMs) are low-cost and accessible modalities linked to brain $A\beta$ variations. However, few have attempted to predict individual-level $A\beta$ -PET spatial patterns using advanced artificial intelligence (AI) systems that jointly leverage MRI and BBMs.

Added value of this study

We proposed a language-guided generative AI model that integrates complementary information from T1-weighted MRI and BBMs for individualized synthesis of $A\beta$ -PET images. The integration process benefits from recent advancements in large language models and prompt engineering. The synthetic PET images exhibited superior visual quality and provided higher diagnostic performance than MRI-based or BBM-based methods alone.

Implications of all the available evidence

Our study suggests that generative AI integrating T1-weighted MRI and BBMs can synthesize high-quality A β -PET images that support AI-based diagnostic workflows with high accuracy. The proposed pipeline, requiring only T1-weighted MRI and BBMs as inputs, is fully automatic, cost-effective, and has the potential to enable large-scale AD screening and precision diagnosis.

1. Introduction

Alzheimer’s disease (AD) is a neurodegenerative disorder causing progressive cognitive and functional decline in patients [1, 2]. Although treatments such as lecanemab and donanemab have shown promise, AD progression remains irreversible [3, 4, 5]. Therefore, timely and accurate diagnosis is essential for effective AD screening and management. To date, amyloid-beta (A β) and tau pathology detection primarily rely on positron emission tomography (PET) imaging and cerebrospinal fluid sampling [6, 7, 8]. In particular, PET imaging remains the only in vivo, non-invasive method capable of providing refined spatial distributions of A β and tau depositions, which are crucial for AD subtyping, staging, and prognosis [9, 10, 11]. However, PET imaging is limited by its high cost, low accessibility, and the potential radiation exposure to patients [12, 13].

To overcome these limitations, generative models have emerged as a promising approach to synthesise realistic PET images from more cost-effective, accessible, and non-radiative data modalities [14, 15]. Previous studies have explored A β -PET synthesis using various data sources, including T1-weighted MRI (T1 images) and functional MRI (fMRI) [16, 17]. T1 images provide high-resolution anatomical details, while fMRI captures dynamic brain activity and functional connectivity. Although both modalities offer clinically relevant information, they are not directly coupled with A β deposition [18, 19]. Consequently, analytical methods based on these modalities often struggle to achieve high-quality, reliable A β -PET synthesis.

Recent advances in blood-based biomarkers (BBMs) offer a sensitive, cost-effective assessment of A β pathology at the global level [20, 21, 22, 23, 24]. BBM-based methods have successfully predicted A β -PET positivity and global standardised uptake value ratios (SUVRs) [25, 26, 27, 28]. Importantly, BBMs are minimally invasive, easy to collect, and inexpensive to apply in clinical settings [29, 27]. However, while BBMs reflect the macroscopic state of A β pathology, they lack spatial resolution and are insufficient

to represent detailed deposition patterns captured by PET imaging. Given the complementary nature of BBMs and MRI, integrating these modalities into a multimodal framework could enable refined, high-quality, and cost-effective A β -PET synthesis.

While T1 images offer detailed spatial information, BBMs are numerical data without inherent spatial context. This modality disparity presents a major challenge for multimodal fusion. Leveraging the capabilities of large medical language models (LLMs) and prompt engineering [30, 31, 32, 33, 34], we introduce a language-enhanced encoder that aligns BBMs with deep clinical knowledge beyond raw numerical representation. Trained on large-scale medical corpora, the LLM captures clinically meaningful semantics. By translating non-imaging data into context-rich representations, we explore prompt-guided LLMs for extracting knowledge-enhanced BBM features. Integrating these with T1-derived spatial features, we enable more effective multimodal generative modelling for AD assessment.

In this study, we propose a language-enhanced generative model based on clinical T1 images and BBMs to synthesise realistic PET images for improved A β spatial pattern assessment. We comprehensively evaluate the synthetic PET images in terms of image quality, diagnostic feature consistency (including physician-based assessment), and clinical applicability using a large cohort (N = 566). The proposed model outperforms conventional methods across all evaluation dimensions, primarily due to its LLM-driven feature enhancement and prompt-based learning strategy. Our results highlight that this generative AI framework provides a cost-effective solution to support large-scale AD screening, diagnosis, and management.

2. METHODS

2.1. *Participants and materials*

2.1.1. *Participants*

Participants for this study were recruited from Huashan Hospital and the Sixth People’s Hospital affiliated with Shanghai Jiao Tong University. The research was approved by the institutional review boards of both hospitals and all participants provided written informed consent. Data collection was registered under the identifier "ChiCTR2000036842" with the title "Construction of a Pre-clinical AD Neuroimaging Cohort Using the ATN System" (<http://www.chictr.org.cn/showproj.aspx?proj=59802>).

Participants were selected according to the following exclusion criteria: 1) fewer than 5 years of education, 2) a history of neurological or psychiatric disorders, 3) other neurological conditions beyond AD spectrum disorders, and 4) significant alcohol or drug abuse. In total, 566 participants were enrolled and data collection commenced in December 2018 and concluded in July 2022. The dataset includes demographic details (age, gender, years of education), MR and PET imaging data, 7 types of BBMs, and results from 8 neuropsychological tests.

2.1.2. MR and PET imaging

T1 images were acquired using a 3T Prisma MRI scanner (Siemens, Erlangen, Germany) at the Shanghai Jiao Tong University Affiliated Sixth People’s Hospital. The imaging was performed with a 3D magnetization-prepared rapid gradient-echo sequence, employing the following parameters: repetition time = 3000 ms, echo time = 2.56 ms, flip angle = 7°, acquisition matrix = 320×320 , in-plane resolution = $0.8 \times 0.8 \text{ mm}^2$, slice thickness = 0.8 mm, and 208 sagittal slices.

A β -PET imaging was performed using a Biograph mCT Flow PET/CT scanner (Siemens Healthineers, Erlangen, Germany) at the Department of Nuclear Medicine & PET Center, Huashan Hospital, Fudan University, within two weeks following the MRI scans [35]. Participants received an intravenous injection of 18F-AV45 at approximately 7.4 MBq/kg. After a 50-minute rest period, they underwent low-dose CT scanning and PET scanning. The PET scans were subsequently processed using a filtered back-projection reconstruction algorithm, which included corrections for decay, normalization, dead time, photon attenuation (based on CT), scatter, and random coincidences. The final PET images had a matrix size of $168 \times 168 \times 148$ voxels and a voxel resolution of $2.04 \times 2.04 \times 1.5 \text{ mm}^3$.

2.1.3. Blood-based biomarkers for AD

We collected plasma samples before PET scans, stored them at -80°C, and subsequently analyzed these samples using the Quanterix Simoa HD-1 platform [23, 25]. The measurement of plasma AD biomarkers included A β 42, A β 40, T-tau (Neurology 3-Plex A assay kit, lot 502838), p-tau181 (Assay Kit V2, lot 502923), and neurofilament light chain (NFL, NF-light assay kit, lot 202700)[36, 37]. The A β 42/40 ratio was calculated as a normalized measure of A β pathology. The p-tau181/A β 42 ratio was computed to assess the relationship between tau phosphorylation and amyloid pathol-

ogy. In addition, NFL concentrations were measured to indicate the level of neurodegeneration. Technicians blinded to clinical imaging data performed the measurements to avoid potential bias. Plasma biomarker concentrations were reported in pg/mL.

2.1.4. Neuropsychological assessment

Systematic neuropsychological assessments (NAs) were conducted by trained neuropsychologists at Shanghai Jiao Tong University Affiliated Sixth People’s Hospital. This evaluation comprised 8 assessments: Mini-Mental State Examination (MMSE), Montreal Cognitive Assessment-Basic (MoCA-B), auditory verbal learning test 30-minute long-delayed free recall (AVLT-LDR), AVLT-recognition (AVLT-R), animal fluency test (AFT), 30-item Boston naming test (BNT), shape trails test A and B (STT-A and STT-B) [38, 39, 40, 41, 42]. We obtained 8 neuropsychological scores from these assessments: MMSE and MoCA-B for global cognitive functions; AVLT-LDR and AVLT-R for memory function; AFT and BNT (total scores) for language function; and STT-A and STT-B (time to completion) for executive function. Higher scores indicate better cognitive ability for all measures except STT-A and STT-B, where shorter completion times reflect better executive function. It should be noted that we have included all available scores to patients. In particular, MMSE and MoCA-B scores were completed by all patients.

The criteria for diagnosing AD dementia (ADD) and mild cognitive impairment (MCI) were derived from the 2011 National Institute on Aging-Alzheimer’s Association (NIA-AA) guidelines for ADD, along with a modified version of Jak and Bondi’s criteria[43, 44]. MCI was identified in participants who showed impairment in one or more cognitive domains or had scores more than one standard deviation below the norm in each of the three cognitive domains[45]. Participants exhibiting no signs of cognitive impairment were classified as cognitively unimpaired (CU).

2.1.5. Data preprocessing

T1 and PET images were preprocessed using Advanced Normalization Tools (ANTs, <https://antspy.readthedocs.io/en/latest/index.html>). For T1 images, N4 bias correction was applied to mitigate bias field effects, followed by skull stripping with a pretrained deep learning method from ANTsPyNet (<https://antspy.readthedocs.io/en/latest/segmentation.html>). PET images were registered to the corresponding T1 images using an affine transformation computed by ANTs after acquisition and reconstruction. The same brain

mask from the T1 images was used to perform skull stripping on the PET images. To convert PET intensity values to SUVR, we normalized them against the average regional value of the bilateral cerebellar crus. These regions were identified using an affine registration from the automated anatomical labeling-116 (AAL-116) atlas, aligning the template T1 brain images to the individual T1 space. All images were then resized to $128 \times 128 \times 128$ voxels and scaled to intensity values between 0 and 1 before being fed into the AI models.

2.2. Language-enhanced generative framework

Figure 1 illustrates our language-enhanced generative framework for synthesizing PET images from T1 images and non-imaging data composed of patient demographics, BBMs, and NAs. The framework comprises two main components: a language-enhanced encoder and a generative adversarial network (GAN). Specifically, the language-enhanced encoder first transforms all non-imaging data into a Global-context Prompt, which summarizes key clinical information, and then encodes this prompt into semantic features using an LLM. The generative adversarial network consists of a generator and a discriminator. The generator takes T1 images and the encoded text features as inputs to produce the corresponding PET images. Meanwhile, the discriminator distinguishes between real and synthetic PET images for adversarial training. To enable effective multimodal integration, two separate text-image fusion modules are respectively designed for the generator and the discriminator.

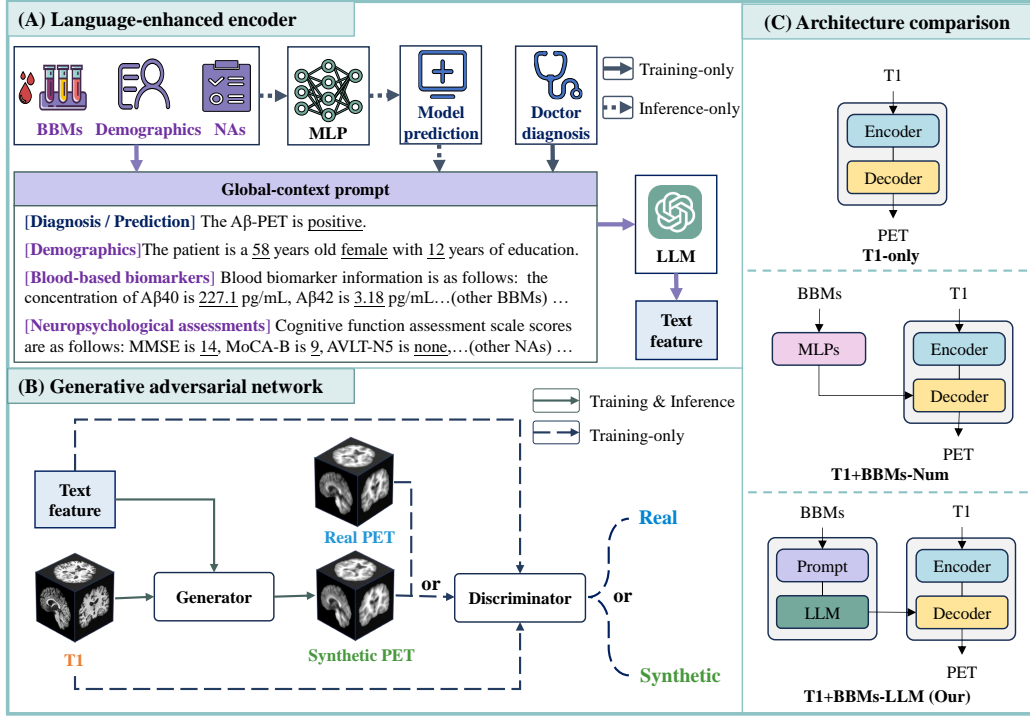


Figure 1: Overview of our proposed language-enhanced generative framework for PET synthesis. **(A) Language-enhanced encoder:** Clinical variables including demographics, BBMs, and NAs are formatted into a global-context prompt, which begins with a global PET characteristics statement (ground-truth diagnosis for training and clinical-variable-based prediction for inference, see Methods), followed by structured clinical details. The prompt is encoded into text features using a medical LLM. **(B) Generative adversarial network:** The generator uses T1 images along with text features to synthesize A β -PET images. The discriminator evaluates the authenticity of PET images by comparing them with paired T1 images and text features only during training stage. **(C) Architecture comparison:** This component illustrates the key differences between our method and two representative baselines. Our approach ("T1+BBMs-LLM") synthesizes PET images using T1-weighted images and BBMs encoded as text features via an LLM. In contrast, the "T1-only" baseline uses only T1 images, while the "T1+BBMs-Num" baseline incorporates BBMs as normalized numerical features.

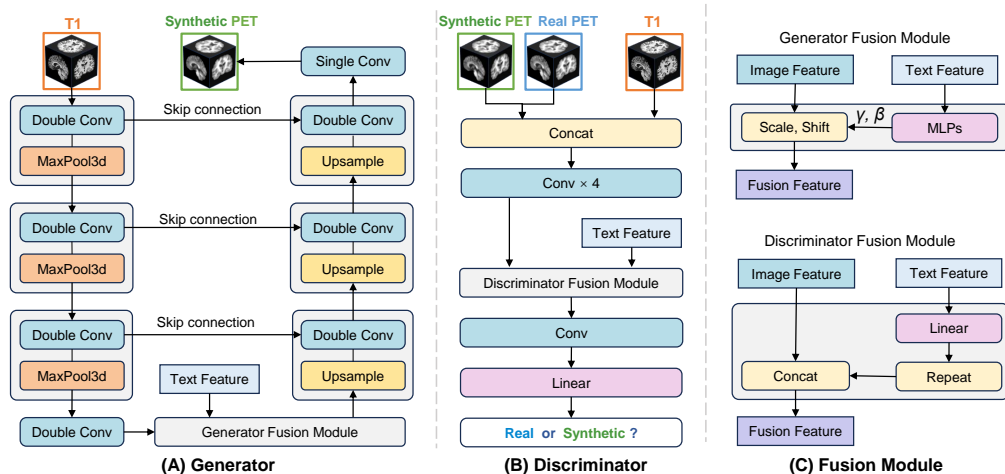


Figure 2: Detailed architecture of the proposed framework. **(A) Generator:** The generator employs a three-layer U-Net architecture. The encoder includes three downsampling blocks with double convolutional layers and max pooling. The encoded T1 features are then fused with text features. The decoder features three upsampling blocks with trilinear interpolation and double convolutional layers, incorporating skip connections to retain feature information. Finally, the decoder output is processed through a convolutional layer to synthesize the PET image. **(B) Discriminator:** The discriminator begins by concatenating the T1 and PET image, followed by feature extraction using four convolutional layers. These image features are integrated with text features. The combined features are subsequently processed through a convolutional layer and a fully connected layer to produce the authenticity judgment for each PET image. **(C) Fusion Module:** In the generator fusion module, text features generate scale and shift parameters through non-linear multilayer perceptrons (MLPs), which adjust image features on a channel-wise basis. In the discriminator fusion module, text features are first reduced in dimensionality through a linear layer, then expanded by repeating the channels to fill the remaining dimensions, and finally concatenated with the image features.

2.2.1. Language-enhanced encoder

The language-enhanced encoder is designed to extract semantic features from a range of clinical variables (BBMs, demographics, and NAs). This process consists of two main stages: (1) transforming these variables into a unified textual format, referred to as the global-context prompt, and (2) encoding this prompt into semantic features using a medical LLM.

Prompt engineering involves mapping numerical clinical variables into structured text, which is crucial for guiding the LLM to produce accurate and refined outputs [46, 47]. To enable this, we design a global-context prompt that combines a summary-level descriptor of A β pathology with a structured

representation of key clinical variables (see “Global-context prompt” in Figure 1). This prompt provides a semantic lead-in to orient the LLM’s interpretation while integrating all relevant inputs into a coherent, language-based format for effective context modeling.

The global-context prompt consists of two components: (i) a summary diagnostic sentence reflecting the overall A β pathology status (e.g., “The A β -PET is positive/negative.”), and (ii) a structured list of 18 clinical variables, including age, gender, years of education, A β 40, A β 42, T-Tau, P-Tau 181, NFL, A β 42/40, P-Tau 181/A β 42, MMSE, MoCA-B, AVLT-N5, AVLT-N7, AFT, BNT, STT-A, and STT-B. To ensure structural consistency, missing values are explicitly denoted as “None”.

During training, the summary sentence is derived from the gold-standard A β -PET diagnosis obtained through expert assessment. In the inference stage, where real PET images and expert evaluations are unavailable, we instead derive a coarse prediction for constructing this summary using a prediction model based on clinical variables. Specifically, a two-layer multilayer perceptron (MLP) is trained to predict A β -PET positivity based on 11 clinical variables, excluding gender and 6 NAs that exhibit substantial missingness. The model’s binary prediction is then used to construct the summary sentence. Notably, this predicted summary serves only as guidance for the LLM and does not explicitly determine the final characteristics of the synthetic PET image. As demonstrated in Section 3.4 and Figure S1, the generated PET images remain capable of capturing realistic A β pathology patterns even when the predicted summaries contain mistakes.

For the feature extraction, we utilize a pretrained BioMedBERT model [48] that specializes in biomedical natural language processing. Trained on a diverse range of biomedical texts (e.g., PubMed), BioMedBERT has a broad knowledge base to encode clinical text information. The model processes text data by first tokenizing it into smaller units of words. These tokens are then analyzed through multiple transformer layers, which capture the context and semantic meaning of the text inputs. This critical design results in the generation of a knowledge-enhanced feature representation of the input clinical texts.

2.2.2. Generator and discriminator

In Figure 2, the generator synthesizes PET images from T1 images and encoded text features, while the discriminator learns to distinguish between real and synthetic PET images. Through iterative optimization of both com-

ponents, we find that the model can progressively improve the quality of the synthetic PET images.

The generator is built using a U-Net architecture, a type of convolutional neural network (CNN) [49]. U-Net features a contracting path (encoder) that captures context through downsampling and feature compression, and a symmetric expanding path (decoder) that enables precise localization through upsampling and feature decompression. Both the encoder and decoder use convolutional layers, with skip connections established between corresponding spatial resolutions. These skip connections transmit features directly to the decoder, preserving finer details in the synthetic PET images. Additionally, the bottleneck layer of the U-Net includes a generator fusion module to integrate T1 features with text features.

The discriminator is a CNN model designed to classify PET images as either synthetic or real classes. We extend the concept of paired adversarial loss [50] to be implemented with three modalities. Along with using synthetic or real PET images as inputs, the discriminator is provided with corresponding T1 images and text features as additional reference information. This design enables the discriminator to reference all available modalities when determining whether a PET image is real or synthetic. Specifically, the discriminator employs four convolutional layers to extract paired features from T1 and PET images, followed by merging these image features with text features in the discriminator fusion module.

The loss function comprises three primary components: the generator loss, the discriminator loss, and the Mean Squared Error (MSE) loss. The generator loss (L_G) is used during the training of generator and is defined as the negative expected value of the log-probability that discriminator assigns to synthetic PET images (where a probability closer to 1 indicates a more realistic image).

$$L_G(G, D) = -\mathbb{E}[\log(D(G(x_1, x_2), x_1, x_2))]. \quad (1)$$

$\mathbb{E}(\cdot)$ denotes the operator of expected value calculation (averaging). $G(x_1, x_2)$ denotes the PET image synthesized by the generator G from T1 image x_1 and text feature x_2 . $D(G(x_1, x_2), x_1, x_2)$ represents the probability assigned by the discriminator D to the synthetic PET being real. Therefore, minimizing L_G means maximizing this probability for all cases. After training, the generator is able to synthesize PET images that can deceive the discriminator.

During the training of the generator, the MSE loss (L_{MSE}) is also used. The MSE loss focuses on the voxel-level similarity between the synthetic and real PET images, complementing the generator loss by addressing details that may be overlooked. L_{MSE} calculates the expected value of the squared difference between corresponding voxels in the synthetic and real PET images.

$$L_{MSE}(G) = \mathbb{E}[(y - G(x_1, x_2))^2], \quad (2)$$

where y denotes the real PET image.

The total generator loss combines L_G and L_{MSE} , weighted by a parameter λ :

$$L_{G_{\text{total}}}(G) = L_G(G, D) + \lambda L_{MSE}(G). \quad (3)$$

During the training of the discriminator, the discriminator loss (L_D) is utilized. The discriminator’s role is to distinguish between real and synthetic PET images. To achieve this, the discriminator loss is defined to maximize the probability that the discriminator assigns to real PET images (maximizing $D(y, x_1, x_2)$) and to minimize the probability assigned to synthetic PET images (maximizing $1 - D(G(x_1, x_2), x_1, x_2)$). Consequently, the discriminator loss is expressed as

$$L_D(G, D) = -\mathbb{E}[\log D(y, x_1, x_2)] - \mathbb{E}[\log(1 - D(G(x_1, x_2), x_1, x_2))]. \quad (4)$$

After training, the discriminator is able to distinguish between real and synthetic PET images, engaging in adversarial training with the generator.

2.2.3. Fusion modules

In Figure 2, we design two fusion modules to integrate text and image features for the generator and discriminator respectively. The discriminator fusion module employs concatenation as previous generative models [51, 52]. This module applies a linear layer to adjust the dimensions of the text features from 756 to 32. These adjusted text features are then repeated to match the dimensions of the image features. Finally, the text and image features are concatenated along the channel dimension. Incorporating text features into the discriminator allows it to utilize these features when assessing the authenticity of PET images, thereby directing the generator to produce PET images that more accurately reflect the text information.

In the generator, we aim to use T1 features as the primary component, with text features serving to modulate them. Consequently, we designed the generator fusion module based on the idea of feature-wise linear modulation [53], rather than employing a concatenation. This module calculates a linear modulation based on the text feature to manipulate the entire image feature, resulting in a fused feature representation. Specifically, we employ two layers of MLPs to estimate scaling parameters (γ) and shifting parameters (β), which match the channel dimensions of the image features. These parameters are used to scale and shift the image features in each channel, facilitating the modulation of image features by the text features.

2.3. Evaluation of synthetic PET images

The PET images synthesized by our model are systematically evaluated from three key perspectives: image quality, diagnostic feature consistency, and clinical applicability. First, image quality is assessed based on the voxel-level and region-level visual resemblance of synthetic PET images to real PET images. Next, diagnostic feature consistency is examined to determine whether the diagnostic information in the synthetic PET images aligns with that in real PET images. Finally, clinical applicability is assessed to evaluate how synthetic PET images can enhance AD assessment in terms of diagnostic performance.

2.3.1. Evaluation of image quality

The quality of synthetic PET images is evaluated from two complementary perspectives. On the one hand, we consider global image quality metrics that are widely used in computer vision. These voxel-level measures focus on the overall similarity between synthetic and real images. Specifically, we calculate the Structural Similarity Index (SSIM), Peak Signal-to-Noise Ratio (PSNR), and Mean Squared Error (MSE) [54]. MSE quantifies the average voxel-wise discrepancy between synthetic and real PET images, PSNR represents the ratio between the meaningful signal and the error, and SSIM jointly assesses similarity in terms of luminance, contrast, and structure. While these global metrics are important for benchmarking generative models, they do not fully capture the clinical utility of PET synthesis.

On the other hand, because PET interpretation is usually performed at the brain region level, we further design region-based evaluation metrics tailored to this application scenario. For each subject, SUVRs are first averaged within anatomically defined regions, including 116 gray-matter regions from

the AAL-116 atlas and four additional white-matter regions segmented using the SynthSeg toolbox [55]. Based on these regional SUVRs, we adopt two complementary measures. First, to assess consistency across regions within each subject, we compute the Pearson correlation coefficient (Pearson’s R) between synthetic and real PET regional SUVRs. This relationship is also visualized using scatter plots with fitted regression lines, providing an intuitive view of inter-region agreement. Second, to examine the distribution of synthesis errors across the brain, we calculate the absolute difference between synthetic and real PET SUVRs for each region and then average these errors across all subjects. This region-level error profile highlights anatomical areas where synthesis is more or less accurate and enables direct comparison between different methods.

In the results, our method is labeled as "T1+BBMs-LLM", which synthesizes PET images using T1-weighted images and BBMs encoded by LLM. We compare the proposed method to two representative baselines: (i) a classic image-to-image generation model using only T1 as input, labeled as "T1-only", and (ii) a model that incorporates BBMs as numerical values, rather than textual data, labeled "T1+BBMs-Num". In the "T1+BBMs-Num" method, BBMs are encoded into normalized numerical values, which are then directly used as features to assist in PET image synthesis.

2.3.2. Evaluation of diagnostic consistency

To ensure that synthetic PET images preserve diagnostically meaningful features beyond visual similarity, we develop a physician-based evaluation to assess diagnostic consistency. This evaluation aims to determine how well physicians can assess A β positivity in synthetic PET images using the same criteria established for real PET images. A high level of agreement between diagnoses based on synthetic and real PET images would suggest that the synthetic images retain critical pathological features relevant for diagnosis.

Given the time and expertise required for manual annotation, this evaluation was performed on a representative subset of 50 cases. We employed a double-reading arbitration workflow: two senior physicians independently assessed the sampled synthetic PET cases, and a third senior physician reviewed and confirmed the final decisions. To ensure representative sampling, the selected subset was chosen to maintain an MSE distribution closely matching that of the overall dataset.

To assess the diagnostic consistency, we first evaluate the agreement between diagnoses based on synthetic and real PET images using Cohen’s

Kappa [56]. This metric directly measures inter-rater reliability, where $0 \leq \text{Kappa} < 0.2$ indicates poor diagnostic consistency, $0.2 \leq \text{Kappa} < 0.6$ indicates moderate consistency, and $\text{Kappa} \geq 0.6$ indicates good consistency. Since this is also a classification task, we evaluate the diagnostic performance using traditional metrics of accuracy, sensitivity, specificity, and F1 score.

Due to the practical limitations of expert review at scale, we complement the physician-based evaluation with an auxiliary model-based evaluation. This approach allows us to extend diagnostic consistency assessment to the full dataset. We train a supervised CNN model to mimic the diagnostic decision-making process of physicians based on real PET images. Once validated on real data, the model is applied to synthetic PET images to infer $A\beta$ positivity based on visual features. By comparing the model’s predictions across real and synthetic PET images, we evaluate whether diagnostic features are consistently preserved. We adopt 3D-ResNet [57] as the backbone of this diagnostic model. The model-based evaluation is designed solely as a supplementary tool to scale consistency analysis and is not used to replace clinical judgment. Detailed implementation and performance results of the model-based evaluation are reported in the supplementary materials.

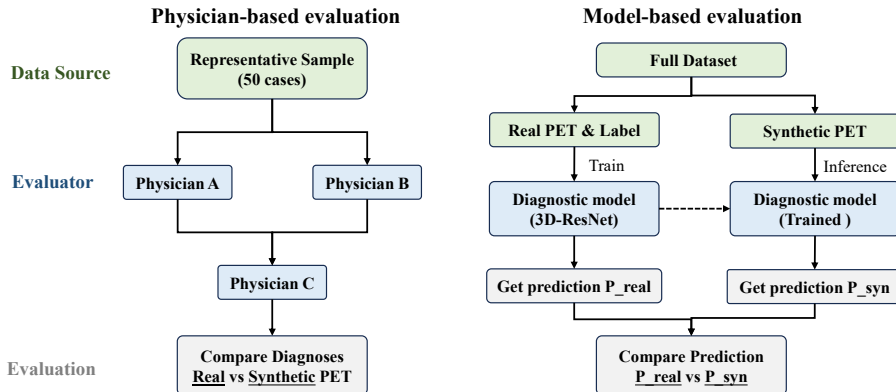


Figure 3: Overview of the diagnostic consistency evaluation framework, which includes two types of assessments—physician-based and model-based—differing in data scope (representative sample vs full dataset) and evaluator (physician vs CNN model)

2.3.3. Evaluation of clinical applicability of fully AI pipeline

To further explore and evaluate the potential of synthetic PET images, we develop an AI diagnostic model based on synthetic images and assess the model performance on the clinical applicability.

In the absence of real PET images, we propose two models to evaluate the utility and scalability of synthetic PET images. The first model relies solely on synthetic PET images, while the second model integrates synthetic PET images with all available clinical assessments to enhance diagnostic performance. The first model is trained based on the 3D-ResNet architecture. The second model employs the well-trained first model for feature extraction from synthetic PET images and the established MLP model (same as described in the LLM-based text encoder section) for feature extraction from clinical assessments. These features are then fused at a logits layer.

We compare these two proposed models with models based on (i) T1, (ii) BBMs, and (iii) a combination of T1 and BBMs. This comparison aims to determine whether synthetic PET images offer advantages in predicting A β positivity and whether they can be further optimized by incorporating additional relevant variables. The evaluation metrics include AUC, accuracy, sensitivity, specificity, and F1 score.

2.4. Implementation

For the generative model, the loss function weight λ is set to 10 to balance the losses. The Adam optimizer is used with an initial learning rate of 5.0e-4 for the generator and 1.0e-4 for the discriminator. The weight decay is set to 1.0e-4, and the parameters for the first and second moment estimates of the gradients, β_1 and β_2 , are set to 0.5 and 0.999, respectively. The learning rate decay strategy employs cosine annealing with a period of 100 epochs and a minimum learning rate of 1.0e-7. Training is conducted for 100 epochs with a batch size of 8.

For the classification model, the initial learning rate is set to 1.0e-4, with the same optimization strategy and number of epochs as the generative model, but with a batch size of 16. All models are initialized using Gaussian initialization (mean = 0, standard deviation = 0.02). Training is implemented using the PyTorch framework and performed on a single NVIDIA GeForce GTX 3090Ti GPU.

2.5. Statistical analysis

Due to the non-normal distribution of the data, differences in gender are tested using Fisher’s exact test, while differences in age, education years, BBMs, and NAs are tested using two-sided Whitney-Mann’s U test. For model validation, the mean and standard deviation (STD) of performance

metrics from cross-validation are computed and reported. Performance metric comparisons between different methods are conducted using one-sided paired t-test. All statistical analyses are performed using python 3.10, scikit-learn 1.5.0 and scipy 1.13.1.

3. RESULTS

Table 1: Participant characteristics

	CU	MCI	ADD
Sample Size	342	134	90
Age (median (IQR))	65.0 (10.0)	66.0 (10.0)	66.0 (11.0)
Females (No. (%))	218 (63.7)	83 (61.9)	52 (57.8)
Education (median (IQR))	12.0 (5.0) b***	11.0 (4.0) a***	9.0 (6.0) c***
A β 40 (pg/mL) (median (IQR))	196.43 (65.3)	193.05 (81.9)	197.40 (59.6)
A β 42 (pg/mL) (median (IQR))	10.2 (4.13) b**	10.3 (4.00)	9.02 (4.26) c**
A β 42/40 rate (median (IQR))	0.05 (0.02) b***	0.05 (0.01)	0.04 (0.01) c***
T-Tau (pg/mL) (median (IQR))	2.20 (1.19)	2.41 (1.28)	2.18 (1.55)
P-Tau 181 (pg/mL) (median (IQR))	1.75 (1.06) b***	1.97 (1.56) a*	3.36 (2.74) c***
NFL (pg/mL) (median (IQR))	12.6 (8.25) b***	14.8 (9.16) a***	19.6 (9.18) c***
P-Tau 181/A β 42 rate (median (IQR))	0.18 (0.12) b***	0.19 (0.17)	0.4 (0.37) c***
MMSE (median (IQR))	28.0 (2.0) b***	27.0 (2.0) a***	18.0 (6.0) c***
MoCA-B (median (IQR))	26.0 (4.0) b***	22.0 (4.0) a***	14.0 (6.0) c***
AVLT-LDR (median (IQR))	5.0 (4.0) b***	2.0 (3.0) a***	0.0 (1.0) c***
AVLT-R (median (IQR))	22.0 (2.0) b***	18.0 (3.0) a***	17.0 (4.5) c**
AFT (median (IQR))	16.0 (5.0) b***	13.0 (4.0) a***	9.0 (5.0) c***
BNT (median (IQR))	25.0 (5.0) b***	21.0 (5.0) a***	19.0 (7.0) c***
STT-A (median (IQR))	44.0 (16.0) b***	51.0 (19.0) a***	75.0 (37.8) c***
STT-B (median (IQR))	117.0 (45.0) b***	147.0 (53.2) a***	190.0 (84.0) c***
A β -PET positivity (No. (%))	110 (32.2) b***	54 (40.3)	72 (80.0) c***

Note: Data are presented as median (M) and interquartile range (IQR) or participant number (n) and percentage (%). Data were compared using a two-tailed Mann–Whitney U test or Fisher’s exact test.

Abbreviations: A β , amyloid- β ; NFL, neurofilament light chain; IQR, interquartile range; MMSE, Mini-Mental State Examination; MoCA-B, Montreal Cognitive Assessment–Basic Version; AVLT, Auditory Verbal Learning Test; AVLT-LDR, delayed free recall of the Auditory Verbal Learning Test; BNT, Boston Naming Test; AFT, Animal Fluency Test; STT, Shape Trails Test.

Significance: (a) Significant difference between CU and MCI; (b) between CU and ADD; (c) between MCI and ADD. *, **, and *** indicate significant differences between two groups after Bonferroni correction, with $p < 0.05$, $p < 0.01$, and $p < 0.001$, respectively.

3.1. Participant characteristics

This study includes 566 participants with three groups: cognitively unimpaired (CU, $n = 342$), mild cognitive impairment (MCI, $n = 134$), and AD

dementia (ADD, $n = 90$). The characteristics of these participants are depicted in Table ???. The age and sex distributions are similar across the groups. The median education level is 12.0 years in the CU group, which is significantly higher than the 11.0 years in both the MCI and ADD groups. Furthermore, the education level in the MCI group is significantly higher than that in the ADD group. Regarding plasma biomarkers, the ADD group exhibited significantly higher levels of p-tau181, NFL, and P-Tau181/A β 42 ratio, as well as markedly lower levels of A β 42 and A β 42/40 ratio compared to the CU and MCI groups. The MCI group also shows significant alterations in p-tau181 and NFL biomarker levels compared to the CU group, although to a lesser degree than the ADD group. Cognitive and functional assessments, including MMSE, MoCA-B, and other 6 NAs (AVLT-LDR, AVLT-recognition, AFT, and BNT) in cognitive sub-domains, demonstrate a clear decline from CU to MCI and ADD. Conversely, STT-A and STT-B exhibit a significant increasing trend across all three groups.

3.2. Evaluation of image quality

We evaluate the quality of the synthetic A β -PET images by assessing both the overall image fidelity and accuracy in different brain regions. Our method (T1+BBMs-LLM) demonstrates superior performance compared to other methods in these aspects.

As shown in Figure 4A, our method achieves the lowest MSE of 0.00235 ± 0.00021 and the highest PSNR of 27.24 ± 0.26 dB, indicating that the synthesized PET images have minimal voxel-level discrepancies from real PET images. In addition, an SSIM of 0.9202 ± 0.0033 further confirms that our method preserves overall structural similarity. The violin plots also show that the distribution of evaluation results is more favorable for our method. Statistical tests support these findings, with our method showing significant improvements across all metrics (MSE: $P = 1.85e-14$ for T1-only and $P = 4.47e-6$ for T1+BBMs-Num; PSNR: $P = 2.46e-37$ for T1-only and $P = 2.90e-11$ for T1+BBMs-Num; SSIM: $P = 7.92e-67$ for T1-only and $P = 0.0067$ for T1+BBMs-Num). Notably, the T1+BBMs-Num method shows improvement over the T1-only method, underscoring the usefulness of incorporating BBMs in synthesizing PET images. However, this approach is limited by numerical encoding. Our method overcomes this limitation by introducing LLM-based encoding, thereby better leveraging BBMs.

Qualitative comparisons are presented in Figure 4B. Each case includes T1 images, real PET images, synthetic PET images generated by three meth-

ods, and corresponding absolute error maps. These cases feature coronal, sagittal, and transverse slices for a comprehensive illustration. PET images synthesized from T1-only inputs mainly preserve structural information but fail to capture pathological uptake patterns, leading to larger errors. The T1+BBMs-Num method improves the representation of A β deposition but still shows noticeable deficiencies in regions such as the frontal, occipital, and temporal lobes (highlighted with boxes and circles). In contrast, our method produces synthetic PET images with spatial patterns closely resembling real PET, reducing both local discrepancies and global error.

To further evaluate region-specific accuracy, we compared synthetic and real PET SUVRs at the level of anatomically defined regions. Our method achieves the strongest correlation, with Pearson’s R of 0.9545 ± 0.0065 , demonstrating robust agreement in regional uptake patterns (Figure 5A). Comparison of individual R among three methods suggest a significant improvement of our method (Pearson’s R: $P = 2.42e-42$ for T1-only and $P = 5.20e-18$ for T1+BBMs-Num). Figure 5B shows the distribution of regional absolute errors across 116 gray-matter and 4 white-matter regions, averaged over all subjects. Our method consistently yields lower errors than the baselines, particularly in regions such as the frontal cortex, temporal lobe, and pre-cuneus—areas known to be clinically relevant for A β deposition. These results further confirm that our method not only improves global similarity but also better captures the spatial distribution of pathological features across the brain.

Figure 5B presents the distribution of regional absolute errors across 116 gray-matter and 4 white-matter regions, averaged over all subjects. Our method provides the lowest discrepancy in regional SUVRs compared with the baselines, highlighting its ability to accurately capture regional A β deposition patterns. Notably, the bilateral cingulum (Cingulum_Mid_L and Cingulum_Mid_R), cerebellar vermis (Vermis_3 and Vermis_4_5), and bilateral thalamus exhibit markedly reduced errors, while consistent improvements are also observed in subcortical structures such as the caudate, putamen, pallidum, and insula bilaterally. These results confirm that our method not only improves global similarity but also more faithfully preserves the spatial distribution of pathological features across the brain.

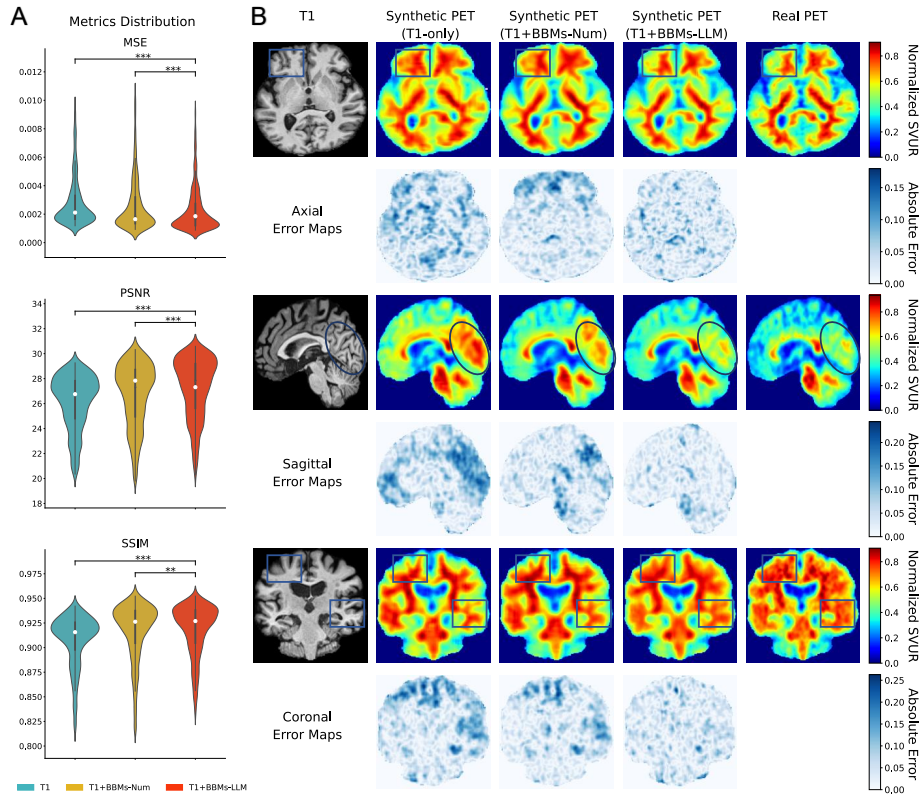


Figure 4: Evaluation of image quality of the synthetic PET image. (A). Violin plots for comparing image quality assessment metrics distributions in individual predictions across methods. **: indicates significance at $P < 0.01$. ***: $P < 0.001$. (B) Visual comparison for investigating the methodological differences through case studies. From left to right, it includes T1, synthetic PET images from three methods, and real PET images. PET images are displayed using range-normalized SUVrs with pseudocolors for clarity. Areas with obvious differences are highlighted with annotations, as boxes or circles, in the images. Below each synthetic PET image, corresponding error maps are provided, indicating discrepancies measured by absolute differences.

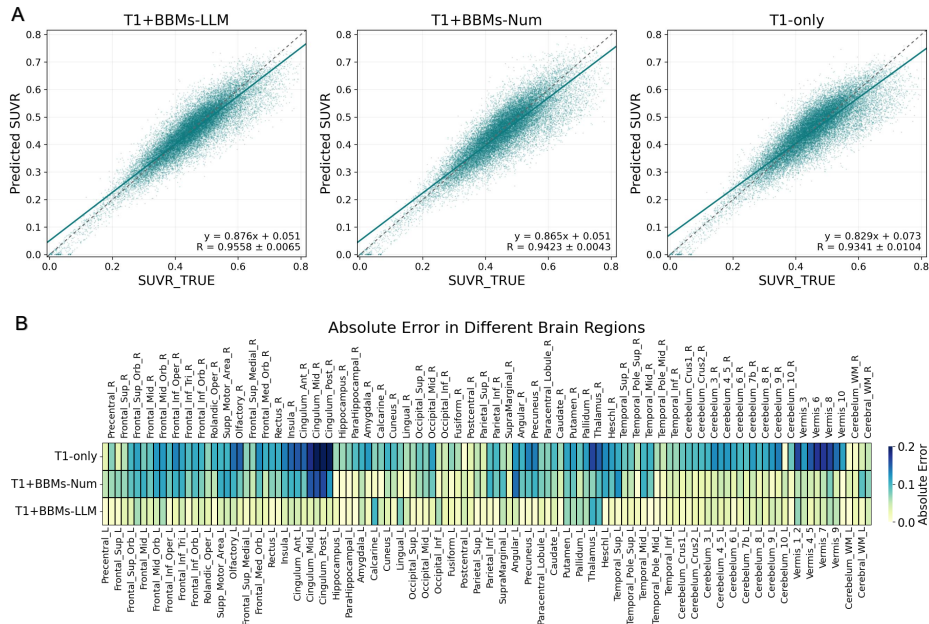


Figure 5: Region-based evaluation metrics for different methods. (A). Scatter plot between ground-truth and predicted regional SUVRs for all subject with inter-region correlations and (B) absolute errors in different brain regions. The brain is divided into 116 gray-matter regions based on the AAL-116 atlas and 4 white-matter regions. The correlation and absolute error between the mean SUVR of the synthetic PET and real PET images for each region are shown. In B, darker colors representing larger errors. Each row corresponds to a method, with the last row representing our method.

3.3. Evaluation of diagnostic consistency

To examine whether synthetic PET images retain diagnostically meaningful features beyond visual similarity, we conducted a physician-based evaluation. As shown in Figure 6A–B, the synthetic PET images achieved an accuracy of 0.80, an F1 score of 0.75, and a Cohen’s Kappa of 0.60. These values indicate good agreement with diagnoses based on real PET images, suggesting that the synthetic images preserve critical pathological features relevant for clinical interpretation. Notably, diagnostic consistency was higher for $A\beta$ -negative cases, with relatively lower performance observed for $A\beta$ -positive cases. This discrepancy likely stems from the greater challenge faced by generative models in accurately capturing and reproducing the subtle pathological signals characteristic of $A\beta$ -positive subjects.

For the model-based evaluation, the judge model trained on real PET images demonstrates strong performance (accuracy of 0.8357 and an AUC

of 0.8768). We see that the judge model captures key diagnostic features in real PET images and is thus well suited for evaluating the diagnostic consistency. Although this result may be influenced by the imperfect accuracy of judge model, it allows for a comparative analysis with our approach evidently outperforming the other two baselines.

Figures 6C-E further illustrate the diagnostic results inferred by the judge model. We recognize that the T1-only method performs poorly across all metrics, with an F1 score and sensitivity below 0.7, and T1+BBMs-Num performs slightly better (merely above 0.7). These results indicate that the PET images synthesized by these methods remarkably differ from real PET images in terms of the diagnostic features. In contrast, our method achieves the leading values in all metrics, reflecting the strength of our diagnostic consistency to the real PET. For instance, our method outperforms the two compared methods in accuracy ($P = 0.0015$ for T1-only and $P = 0.0060$ for T1+BBMs-LLM) and AUC ($P = 0.0021$ for T1-only and $P = 0.0236$ for T1+BBMs-LLM). Considering the class imbalance, the F1 score is another important evaluation metric. Our method also shows an improvement over the competing methods ($P = 0.0135$ for T1-only and $P = 0.0532$ for T1+BBMs-Num). The agreement matrices for these results are shown in Figure 6 E. Our method achieves the highest Cohen’s Kappa among all competing methods. Note that the Cohen’s Kappa in this analysis is slightly lower than that using human-based evaluation, which is induced by the imperfect diagnosis ability of the judge model. Overall, though being partially biased, the model-based evaluation offers reasonable evidence supporting the advantage of our method in terms of consistent diagnostic feature generation, which is in line with the image quality metrics analysis.

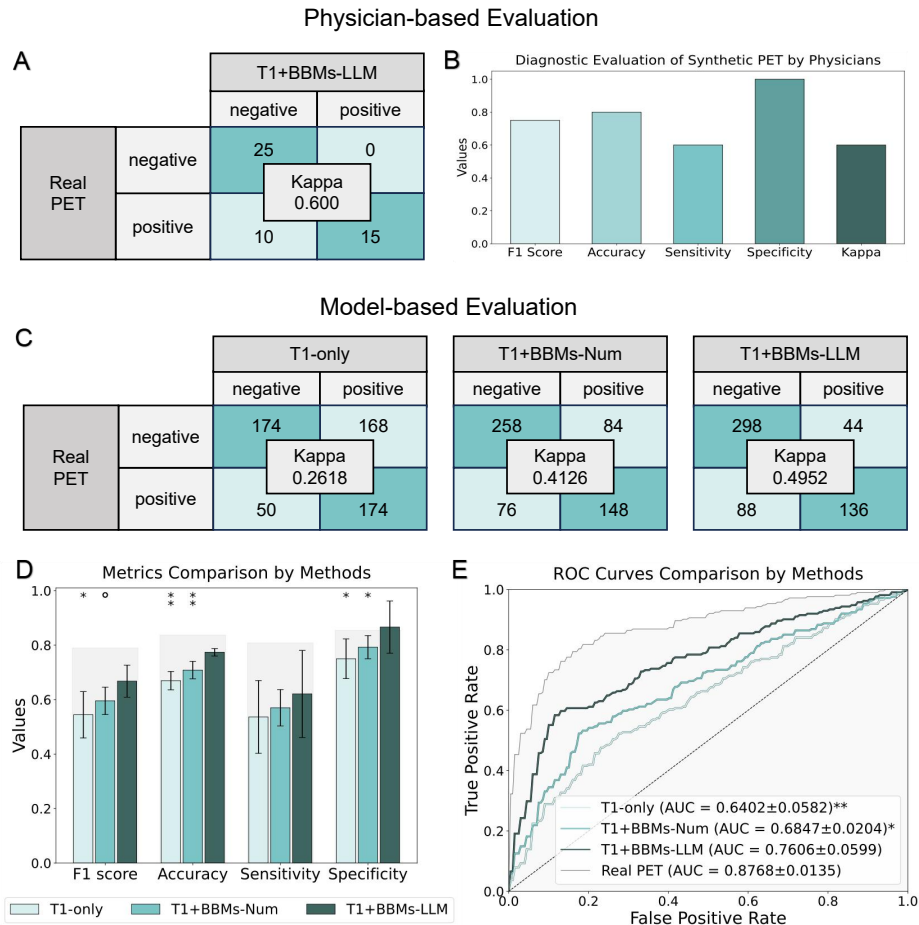


Figure 6: Evaluation on diagnostic consistency of the synthetic PET image. (A-B) The corresponding results of physician-based evaluation. Only results from our method participant this analysis. (A) Inter-rater agreement matrices for real PET and the corresponding synthetic PET from our method, evaluated by physicians. (B) Bar charts of performance metrics of our synthetic PET in physician-based evaluation. (C-E) The performance of PET synthesized by three methods, evaluated by a model trained on real PET. (C) The inter-rater agreement matrix comparing diagnosis of real and synthetic PET, with Cohen’s kappa in the central box. (D) Bar charts showing the F1 score, accuracy, and sensitivity of the three methods, represented by their means with error bars indicating standard deviations. (E) Receiver operating characteristic (ROC) curves and the corresponding AUCs. The performance of real PET is shown with a grey border as a reference. *: indicates significance at $P < 0.05$. **: $P < 0.01$. \circ : a marginal significance, where the P-value is 0.0532.

3.4. Evaluation of clinical applicability of fully AI pipeline

We utilize the synthetic PET images to train A β pathology classification models, establishing a complete AI pipeline to further facilitate the clinical applicability of PET generation. We use T1 images and BBMs to diagnose A β positivity, as comparison baselines. As shown in Figure 7, T1 achieves a classification AUC of only 0.64, with other metrics also performing poorly. BBMs yields slightly better results but with a higher rate of false negatives. Combining T1 images and BBMs using a multimodal diagnostic model improves all metrics, yet this approach still falls short compared to our synthetic PET images. This finding indicates that integrating T1 and BBMs through PET generation model offers a more cohesive fusion for AD diagnosis compared to traditional multimodal diagnostic models. Furthermore, fusing synthetic PET with BBMs yields superior results that outperforms single-modal approaches or their simple fusion (T1, BBMs, and T1+BBMs). Also, the model integrating synthetic PET and BBMs demonstrates a balanced sensitivity and specificity. These findings underscore the potential of synthetic PET from our proposed method in AD diagnostics, particularly in enhancing pathological diagnosis accuracy by integrating diverse sources of clinical information.

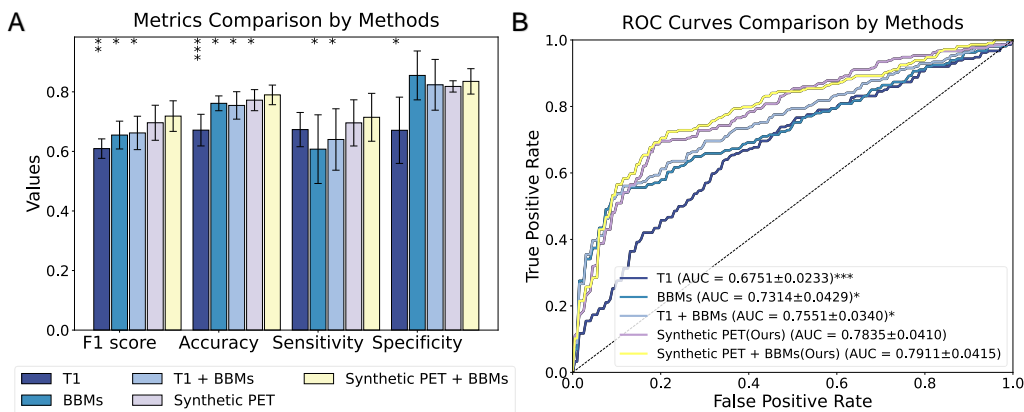


Figure 7: Evaluation results on clinical applicability of the synthetic PET image. (A) Bar charts of F1 score, accuracy, and sensitivity, with error bars indicating standard deviations. (B) ROC curves with the corresponding AUCs. For both plots, the significant differences are annotated for the fusion of synthetic PET and BBMs compared to other methods. *: indicates significance at $P < 0.05$. **: $P < 0.01$. ***: $P < 0.001$.

3.5. The effectiveness of prompt engineering

The prompt engineering for utilizing multi-modality clinical data (e.g., demographics, BBMs and NAs) is a core contribution in our study. We demonstrate the effectiveness of the proposed prompt design using a comparison to three variants in the prompt. In Figure 8 A and B, we observe a remarkable performance decrease when placing the summary sentence (the diagnosis/prediction prompt in Figure 1A) at the end of the prompt. Also, excluding the diagnostic sentence degrades all metrics. However, using the summary sentence only does not result in leading performance, which suggests the key descriptions about the clinical variables are informative. Overall, we recognize that using the summary sentence in starting a prompt can efficiently guide the LLM to encode clinical variables and enhance the quality of synthetic PET images.

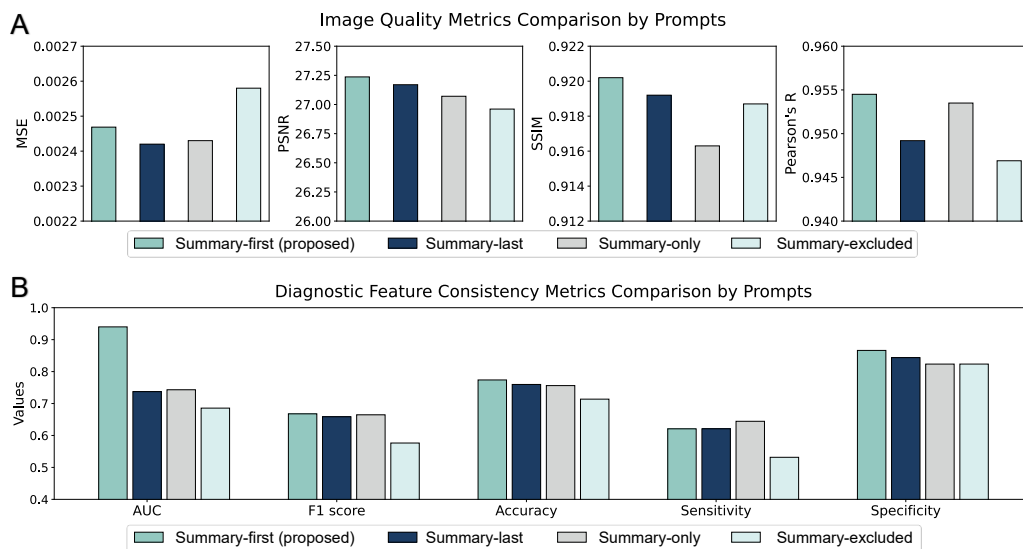


Figure 8: Ablation study for the effectiveness of prompt engineering. Evaluation of (A) PET image quality and (B) diagnostic feature consistency using our proposed prompt and three different prompts for comparisons. The results in B is obtained using model-based feature consistency evaluation. "Summary-first" indicates our proposed design. "Summary-last" places the summary sentence at the end. "Summary-only" uses only the summary sentence. "Summary-excluded" does not include the summary sentence and preserves all other prompts about the clinical variables.

4. Discussion

In this study, we propose a multimodal generative AI approach for synthesizing PET images from structural MRI and BBMs. We develop a language-enhanced framework and prompt engineering to optimize PET synthesis. Our systematic validation shows that the proposed method can (i) produce synthesized PET semantically similar to real-world PET at individual level; (ii) offer consistent A β pathological features to support clinical assessment; and (iii) enable the development of fully AI pipeline to provide A β diagnosis without requiring real-world PET scans.

Achieving a cost-effective and accurate AD diagnosis remains a significant challenge. Routine diagnosis using A β -PET scans is heavily constrained by the cost, availability, and risk of radiation exposure [12, 13]. Meanwhile, BBM-based methods provide a more accessible alternative for predicting AD positivity without requiring PET scans, but the lack of spatial information in BBMs limits their ability to fully replace PET imaging [58, 59]. Our multimodal framework integrates pathological insights from BBM features and T1-based anatomical details to synthesize high-quality A β -PET images. Our validation demonstrates that these images not only provide the spatial information necessary for accurate AD assessments, but also enable the development of AD diagnostic models that outperform the BBM-based methods. Additionally, integrating synthetic A β -PET images with BBMs further enhances diagnostic accuracy, highlighting the potential of generative models to improve AD diagnosis. Overall, our study opens avenues to synthesize PET images from MRI data and BBMs towards predictive AD diagnosis. This data-driven approach is extensible to large-scale early AD diagnosis by offering a cost-effective alternative to real PET imaging.

Our approach is pioneering in integrating BBMs into a multimodal generative model for PET synthesis. We show that the BBM-detected pathological insights can enhance the synthesis of A β -PET spatial pattern, complementing to traditional MRI-based generative approaches. We advance the representation of BBMs by employing a language-enhanced encoder, thereby improving the integration of non-imaging data with T1 images and enhancing PET synthesis. Conventionally, BBMs and other clinical variables were encoded as numerical formats (e.g. concentration levels of BBMs) [60, 61]. A simple integration of high-dimensional image features (more than 10 thousands) and low dimensional non-image BBM features (represented as a few numbers) would likely results in a performance biased towards the image features

[62], which limits the contribution of non-imaging features. In contrast, our approach employs prompt engineering to map non-imaging data into meaningful contexts, guiding a medical LLM to extract knowledge-enhanced features. To improve the context understanding, we design a "summary-first" prompt that prioritizes the critical diagnostic information. Experimental results demonstrate that this design enhances the quality of synthetic PET images, highlighting that a specialized prompt design can greatly contribute to the overall performance.

A key contribution of our study is to enable a systematic process of PET images synthesis and clinical application evaluation. Our comprehensive evaluation is a progressive process, encompassing image quality, diagnostic consistency, and clinical applicability. By contrast, prior PET image synthesis studies have primarily focused on metrics of visual quality (e.g., MSE, PSNR, and SSIM) [14, 15, 16]. It becomes increasingly evident that the detailed depiction of anatomical structures and image-based pathological characteristics are crucial in clinical decision making that are beyond the scope of traditional metrics. In our study, recognizing that PET analysis is frequently performed at the brain-regional level, we introduce key evaluation metrics based on regional SUVs, including an absolute error and inter-region correlation. These metrics ensure a clinically-meaningful structural similarity between synthetic PET images and real PET images. Additionally, physician-based evaluation of image-based pathological characteristics can help assess the effectiveness of synthetic PET images under a clinical setting. However, a physician-based evaluation over large-scale data is time-consuming and labor-intensive. To respond, we perform a physician-based evaluation on a subset of the data and conducted model evaluation on the entire dataset. For the model evaluation, we develop an AI model that can mimic human diagnostic criteria and offer quality insights into the PET image generation. Finally, we establish a fully AI-driven pipeline, consisting of PET generation and AI diagnosis, to substantially confirm the clinical applicability of the proposed method.

Our study has several limitations. First, due to the difficulty in multi-modal data acquisition, our study has not undergone a multi-center systematic evaluation. In addition, the range of the BBM values could vary across the assays and reference protocols [63] and a quality assessment is required to reveal potential protocol-induced BBM variances. Moreover, integrative analysis with other promising biomarkers is valuable to extend the generalization power of our approach. For instance, P-Tau 217 is suggested to

predict continuous brain A β levels in early AD subjects [58] and is recommended as the only BBM to diagnose A β pathology in the NIA-AA 2024 Diagnostic Guidelines [6]. Inclusion of P-Tau 217 into our framework could help achieve the performance improvement. Finally, considering the association of Tau-PET with T1 and BBM [64, 65], the extensive structure of our framework could be adapted for Tau-PET synthesis to facilitate rapid AD staging and prognosis.

In conclusion, our research presents a language-enhanced, multimodal framework that effectively synthesizes A β -PET images from T1 images and BBMs. This advancement addresses critical limitations of traditional PET imaging data, offering a cost-effective and accurate alternative that enhances early AD assessment, diagnosis, and decision making.

Author contributions

ZZ and XM are major contributors to draft and revise of the manuscript for content and to analyze the data. XM, QG, QH and FX played major role in the acquisition of data. ZZ, XM, QG, SZ, QH, MZ, and ML substantially revise the manuscript. ZZ, QH, MZ, ML and FX conceptualize and design the study. ZZ, XM, QH, MZ, and ML interpret the data.

Acknowledgments

This study is supported in part by the National Natural Science Foundation of China (82402394, 82201583, 8217052097, 82071962), Shanghai Pujiang Program (23PJ1430200), STI2030-Major Projects (022ZD0213800), and Shanghai Artificial Intelligence Laboratory.

Financial disclosure

None reported.

Conflict of interest

All authors declare no potential conflict of interests.

Appendix A. Example Appendix Section

Appendix text.

References

- [1] P. Scheltens, B. De Strooper, M. Kivipelto, H. Holstege, G. Chételat, C. E. Teunissen, J. Cummings, W. M. van der Flier, Alzheimer's disease, *The Lancet* 397 (10284) (2021) 1577–1590.
- [2] C. L. Masters, R. Bateman, K. Blennow, C. C. Rowe, R. A. Sperling, J. L. Cummings, Alzheimer's disease, *Nature reviews disease primers* 1 (1) (2015) 1–18.
- [3] D. P. Veitch, M. W. Weiner, P. S. Aisen, L. A. Beckett, N. J. Cairns, R. C. Green, D. Harvey, C. R. Jack Jr, W. Jagust, J. C. Morris, et al., Understanding disease progression and improving alzheimer's disease clinical trials: Recent highlights from the alzheimer's disease neuroimaging initiative, *Alzheimer's & Dementia* 15 (1) (2019) 106–152.
- [4] C. H. Van Dyck, C. J. Swanson, P. Aisen, R. J. Bateman, C. Chen, M. Gee, M. Kanekiyo, D. Li, L. Reyderman, S. Cohen, et al., Lecanemab in early alzheimer's disease, *New England Journal of Medicine* 388 (1) (2023) 9–21.
- [5] S. Srivastava, R. Ahmad, S. K. Khare, Alzheimer's disease and its treatment by different approaches: A review, *European Journal of Medicinal Chemistry* 216 (2021) 113320.
- [6] C. R. Jack Jr, S. J. Andrews, T. G. Beach, T. Buracchio, B. Dunn, A. Graf, O. Hansson, C. Ho, W. Jagust, E. McDade, et al., Revised criteria for the diagnosis and staging of alzheimer's disease, *Nature medicine* (2024) 1–4.
- [7] W. M. Van Der Flier, P. Scheltens, The atn framework—moving pre-clinical alzheimer disease to clinical relevance, *JAMA neurology* 79 (10) (2022) 968–970.
- [8] C. R. Jack Jr, D. A. Bennett, K. Blennow, M. C. Carrillo, B. Dunn, S. B. Haeberlein, D. M. Holtzman, W. Jagust, F. Jessen, J. Karlawish, et al., NIA-AA research framework: toward a biological definition of alzheimer's disease, *Alzheimer's & Dementia* 14 (4) (2018) 535–562.
- [9] D. Biel, M. Brendel, A. Rubinski, K. Buerger, D. Janowitz, M. Dichgans, N. Franzmeier, A. D. N. I. (ADNI), Tau-pet and in vivo braak-staging

- as prognostic markers of future cognitive decline in cognitively normal to demented individuals, *Alzheimer's research & therapy* 13 (1) (2021) 137.
- [10] N. Mattsson, S. Palmqvist, E. Stomrud, J. Vogel, O. Hansson, Staging β -amyloid pathology with amyloid positron emission tomography, *JAMA neurology* 76 (11) (2019) 1319–1329.
- [11] R. Ossenkoppele, R. Smith, N. Mattsson-Carlsson, C. Groot, A. Leuzy, O. Strandberg, S. Palmqvist, T. Olsson, J. Jögi, E. Stormrud, et al., Accuracy of tau positron emission tomography as a prognostic marker in preclinical and prodromal alzheimer disease: a head-to-head comparison against amyloid positron emission tomography and magnetic resonance imaging, *JAMA neurology* 78 (8) (2021) 961–971.
- [12] L. Rice, S. Bisdas, The diagnostic value of fdg and amyloid pet in alzheimer's disease—a systematic review, *European journal of radiology* 94 (2017) 16–24.
- [13] A. Nordberg, J. O. Rinne, A. Kadir, B. Långström, The use of pet in alzheimer disease, *Nature Reviews Neurology* 6 (2) (2010) 78–87.
- [14] S. Hu, B. Lei, S. Wang, Y. Wang, Z. Feng, Y. Shen, Bidirectional mapping generative adversarial networks for brain mr to pet synthesis, *IEEE Transactions on Medical Imaging* 41 (1) (2021) 145–157.
- [15] J. Zhang, X. He, L. Qing, F. Gao, B. Wang, Bpgan: Brain pet synthesis from mri using generative adversarial network for multi-modal alzheimer's disease diagnosis, *Computer Methods and Programs in Biomedicine* 217 (2022) 106676.
- [16] F. Vega, A. Addeh, A. Ganesh, E. E. Smith, M. E. MacDonald, Image translation for estimating two-dimensional axial amyloid-beta pet from structural mri, *Journal of Magnetic Resonance Imaging* 59 (3) (2024) 1021–1031.
- [17] C. Li, M. Liu, J. Xia, L. Mei, Q. Yang, F. Shi, H. Zhang, D. Shen, Individualized assessment of brain $a\beta$ deposition with fmri using deep learning, *IEEE Journal of Biomedical and Health Informatics* (2023).

- [18] C. R. Jack, D. S. Knopman, W. J. Jagust, L. M. Shaw, P. S. Aisen, M. W. Weiner, R. C. Petersen, J. Q. Trojanowski, Hypothetical model of dynamic biomarkers of the alzheimer’s pathological cascade, *The Lancet Neurology* 9 (1) (2010) 119–128.
- [19] S. A. Hasani, M. Mayeli, M. A. Salehi, R. Barzegar Parizi, A systematic review of the association between amyloid- β and τ pathology with functional connectivity alterations in the alzheimer dementia spectrum utilizing pet scan and rsfmri, *Dementia and Geriatric Cognitive Disorders Extra* 11 (2) (2021) 78–90.
- [20] M. M. Mielke, N. R. Fowler, Alzheimer disease blood biomarkers: considerations for population-level use, *Nature Reviews Neurology* (2024) 1–10.
- [21] O. Hansson, R. M. Edelmayer, A. L. Boxer, M. C. Carrillo, M. M. Mielke, G. D. Rabinovici, S. Salloway, R. Sperling, H. Zetterberg, C. E. Teunissen, The alzheimer’s association appropriate use recommendations for blood biomarkers in alzheimer’s disease, *Alzheimer’s & Dementia* 18 (12) (2022) 2669–2686.
- [22] O. Hansson, K. Blennow, H. Zetterberg, J. Dage, Blood biomarkers for alzheimer’s disease in clinical practice and trials, *Nature Aging* 3 (5) (2023) 506–519.
- [23] B. Olsson, R. Lautner, U. Andreasson, A. Öhrfelt, E. Portelius, M. Bjerke, M. Hölttä, C. Rosén, C. Olsson, G. Strobel, et al., Csf and blood biomarkers for the diagnosis of alzheimer’s disease: a systematic review and meta-analysis, *The Lancet Neurology* 15 (7) (2016) 673–684.
- [24] C. E. Teunissen, I. M. Verberk, E. H. Thijssen, L. Vermunt, O. Hansson, H. Zetterberg, W. M. van der Flier, M. M. Mielke, M. Del Campo, Blood-based biomarkers for alzheimer’s disease: towards clinical implementation, *The Lancet Neurology* 21 (1) (2022) 66–77.
- [25] S. Janelidze, N. Mattsson, S. Palmqvist, R. Smith, T. G. Beach, G. E. Serrano, X. Chai, N. K. Proctor, U. Eichenlaub, H. Zetterberg, et al., Plasma p-tau181 in alzheimer’s disease: relationship to other biomarkers, differential diagnosis, neuropathology and longitudinal progression to alzheimer’s dementia, *Nature medicine* 26 (3) (2020) 379–386.

- [26] N. R. Barthélemy, G. Salvadó, S. E. Schindler, Y. He, S. Janelidze, L. E. Collij, B. Saef, R. L. Henson, C. D. Chen, B. A. Gordon, et al., Highly accurate blood test for alzheimer’s disease is similar or superior to clinical cerebrospinal fluid tests, *Nature medicine* 30 (4) (2024) 1085–1095.
- [27] M. R. Meyer, K. M. Kirmess, S. Eastwood, T. L. Wenthe-Roth, F. Irvin, M. S. Holubasch, V. Venkatesh, I. Fogelman, M. Monane, L. Hanna, et al., Clinical validation of the precivityad2 blood test: A mass spectrometry-based test with algorithm combining p-tau_{217} and $\text{a}\beta_{42}/40$ ratio to identify presence of brain amyloid, *Alzheimer’s & Dementia* (2024).
- [28] J. K. Wisch, B. A. Gordon, A. H. Boerwinkle, P. H. Luckett, J. G. Bollinger, V. Ovod, Y. Li, R. L. Henson, T. West, M. R. Meyer, et al., Predicting continuous amyloid pet values with csf and plasma $\text{a}\beta_{42}/\text{a}\beta_{40}$, *Alzheimer’s & Dementia: Diagnosis, Assessment & Disease Monitoring* 15 (1) (2023) e12405.
- [29] S. Palmqvist, P. Tideman, N. Mattsson-Carlgrén, S. E. Schindler, R. Smith, R. Ossenkoppele, S. Calling, T. West, M. Monane, P. B. Verghese, et al., Blood biomarkers to detect alzheimer disease in primary care and secondary care, *JAMA* (2024).
- [30] Y. Zhang, J. Gao, Z. Tan, L. Zhou, K. Ding, M. Zhou, S. Zhang, D. Wang, Data-centric foundation models in computational healthcare: A survey, *arXiv preprint arXiv:2401.02458* (2024).
- [31] K. Singhal, S. Azizi, T. Tu, S. S. Mahdavi, J. Wei, H. W. Chung, N. Scales, A. Tanwani, H. Cole-Lewis, S. Pfohl, et al., Large language models encode clinical knowledge, *Nature* 620 (7972) (2023) 172–180.
- [32] A. J. Thirunavukarasu, D. S. J. Ting, K. Elangovan, L. Gutierrez, T. F. Tan, D. S. W. Ting, Large language models in medicine, *Nature medicine* 29 (8) (2023) 1930–1940.
- [33] J. Wang, E. Shi, S. Yu, Z. Wu, C. Ma, H. Dai, Q. Yang, Y. Kang, J. Wu, H. Hu, et al., Prompt engineering for healthcare: Methodologies and applications, *arXiv preprint arXiv:2304.14670* (2023).

- [34] A. Ahmed, X. Zeng, R. Xi, M. Hou, S. A. Shah, Med-prompt: A novel prompt engineering framework for medicine prediction on free-text clinical notes, *Journal of King Saud University-Computer and Information Sciences* 36 (2) (2024) 101933.
- [35] S. Ren, J. Li, L. Huang, Q. Huang, K. Chen, J. Hu, F. Jessen, X. Hu, D. Jiang, L. Zhu, et al., Brain functional alterations and association with cognition in people with preclinical subjective cognitive decline and objective subtle cognitive difficulties, *Neuroscience* 513 (2023) 137–144.
- [36] F.-F. Pan, Q. Huang, Y. Wang, Y.-F. Wang, Y.-H. Guan, F. Xie, Q.-H. Guo, Non-linear character of plasma amyloid beta over the course of cognitive decline in alzheimer’s continuum, *Frontiers in Aging Neuroscience* 14 (2022) 832700.
- [37] H. Chu, C. Huang, Y. Guan, F. Xie, M. Chen, Q. Guo, The associations between nutritional status and physical frailty and alzheimer’s disease plasma biomarkers in older cognitively unimpaired adults with positive of amyloid- β pet, *Clinical Nutrition* 43 (7) (2024) 1647–1656.
- [38] Q. Guo, Q. Zhao, M. Chen, D. Ding, Z. Hong, A comparison study of mild cognitive impairment with 3 memory tests among chinese individuals, *Alzheimer Disease & Associated Disorders* 23 (3) (2009) 253–259.
- [39] Q. Zhao, Q. Guo, Z. Hong, Clustering and switching during a semantic verbal fluency test contribute to differential diagnosis of cognitive impairment, *Neuroscience bulletin* 29 (2013) 75–82.
- [40] Q. Zhao, Q. Guo, F. Li, Y. Zhou, B. Wang, Z. Hong, The shape trail test: application of a new variant of the trail making test, *PloS one* 8 (2) (2013) e57333.
- [41] Q. Zhao, Q. Guo, X. Liang, M. Chen, Y. Zhou, D. Ding, Z. Hong, Auditory verbal learning test is superior to rey-osterrieth complex figure memory for predicting mild cognitive impairment to alzheimer’s disease, *Current Alzheimer Research* 12 (6) (2015) 520–526.
- [42] D. Ding, Q. Zhao, Q. Guo, X. Liang, J. Luo, L. Yu, L. Zheng, Z. Hong, S. A. S. SAS, Progression and predictors of mild cognitive impairment in chinese elderly: a prospective follow-up in the shanghai aging study,

Alzheimer's & Dementia: Diagnosis, Assessment & Disease Monitoring
4 (2016) 28–36.

- [43] G. M. McKhann, D. S. Knopman, H. Chertkow, B. T. Hyman, C. R. Jack Jr, C. H. Kawas, W. E. Klunk, W. J. Koroshetz, J. J. Manly, R. Mayeux, et al., The diagnosis of dementia due to alzheimer's disease: Recommendations from the national institute on aging-alzheimer's association workgroups on diagnostic guidelines for alzheimer's disease, *Alzheimer's & dementia* 7 (3) (2011) 263–269.
- [44] T. Chen, F. Pan, Q. Huang, G. Xie, X. Chao, L. Wu, J. Wang, L. Cui, T. Sun, M. Li, et al., Metabolic phenotyping reveals an emerging role of ammonia abnormality in alzheimer's disease, *Nature Communications* 15 (1) (2024) 3796.
- [45] L. Huang, K. Chen, Z. Liu, Q. Guo, A conceptual framework for research on cognitive impairment with no dementia in memory clinic, *Current Alzheimer Research* 17 (6) (2020) 517–525.
- [46] P. Sahoo, A. K. Singh, S. Saha, V. Jain, S. Mondal, A. Chadha, A systematic survey of prompt engineering in large language models: Techniques and applications, *arXiv preprint arXiv:2402.07927* (2024).
- [47] V. Liu, L. B. Chilton, Design guidelines for prompt engineering text-to-image generative models, in: *Proceedings of the 2022 CHI conference on human factors in computing systems, 2022*, pp. 1–23.
- [48] S. Chakraborty, E. Bisong, S. Bhatt, T. Wagner, R. Elliott, F. Mosconi, Biomedbert: A pre-trained biomedical language model for qa and ir, in: *Proceedings of the 28th international conference on computational linguistics, 2020*, pp. 669–679.
- [49] Ö. Çiçek, A. Abdulkadir, S. S. Lienkamp, T. Brox, O. Ronneberger, 3d u-net: learning dense volumetric segmentation from sparse annotation, in: *Medical Image Computing and Computer-Assisted Intervention–MICCAI 2016: 19th International Conference, Athens, Greece, October 17–21, 2016, Proceedings, Part II* 19, 2016, pp. 424–432.
- [50] M. Mirza, S. Osindero, Conditional generative adversarial nets, *arXiv preprint arXiv:1411.1784* (2014).

- [51] S. Reed, Z. Akata, X. Yan, L. Logeswaran, B. Schiele, H. Lee, Generative adversarial text to image synthesis, in: International conference on machine learning, 2016, pp. 1060–1069.
- [52] H. Zhang, T. Xu, H. Li, S. Zhang, X. Wang, X. Huang, D. N. Metaxas, Stackgan++: Realistic image synthesis with stacked generative adversarial networks, *IEEE transactions on pattern analysis and machine intelligence* 41 (8) (2018) 1947–1962.
- [53] E. Perez, F. Strub, H. De Vries, V. Dumoulin, A. Courville, Film: Visual reasoning with a general conditioning layer, in: Proceedings of the AAAI conference on artificial intelligence, Vol. 32, 2018.
- [54] A. Hore, D. Ziou, Image quality metrics: Psnr vs. ssim, in: 2010 20th international conference on pattern recognition, 2010, pp. 2366–2369.
- [55] B. Billot, D. N. Greve, O. Puonti, A. Thielscher, K. Van Leemput, B. Fischl, A. V. Dalca, J. E. Iglesias, et al., Synthseg: Segmentation of brain mri scans of any contrast and resolution without retraining, *Medical image analysis* 86 (2023) 102789.
- [56] J. Cohen, A coefficient of agreement for nominal scales, *Educational and psychological measurement* 20 (1) (1960) 37–46.
- [57] S. Chen, K. Ma, Y. Zheng, Med3d: Transfer learning for 3d medical image analysis, *arXiv preprint arXiv:1904.00625* (2019).
- [58] V. Devanarayan, T. Doherty, A. Charil, P. Sachdev, Y. Ye, L. K. Murali, D. A. Llano, J. Zhou, L. Reyderman, H. Hampel, et al., Plasma ptau217 predicts continuous brain amyloid levels in preclinical and early alzheimer’s disease, *Alzheimer’s & Dementia* (2024).
- [59] W. S. Brum, N. C. Cullen, J. Therriault, S. Janelidze, N. Rahmouni, J. Stevenson, S. Servaes, A. L. Benedet, E. R. Zimmer, E. Stomrud, et al., A blood-based biomarker workflow for optimal tau-pet referral in memory clinic settings, *Nature Communications* 15 (1) (2024) 2311.
- [60] T. Xia, A. Chartsias, C. Wang, S. A. Tsiftaris, A. D. N. Initiative, et al., Learning to synthesise the ageing brain without longitudinal data, *Medical Image Analysis* 73 (2021) 102169.

- [61] T. Xia, A. Chartsias, S. A. Tsiftaris, A. D. N. Initiative, Consistent brain ageing synthesis, in: Medical Image Computing and Computer Assisted Intervention–MICCAI 2019: 22nd International Conference, Shenzhen, China, October 13–17, 2019, Proceedings, Part IV 22, 2019, pp. 750–758.
- [62] C. Cui, H. Yang, Y. Wang, S. Zhao, Z. Asad, L. A. Coburn, K. T. Wilson, B. A. Landman, Y. Huo, Deep multimodal fusion of image and non-image data in disease diagnosis and prognosis: a review, *Progress in Biomedical Engineering* 5 (2) (2023) 022001.
- [63] C. Giangrande, V. Delatour, U. Andreasson, K. Blennow, J. Gobom, H. Zetterberg, Harmonization and standardization of biofluid-based biomarker measurements for at (n) classification in alzheimer’s disease, *Alzheimer’s & Dementia: Diagnosis, Assessment & Disease Monitoring* 15 (3) (2023) e12465.
- [64] J. Lee, B. J. Burkett, H.-K. Min, M. L. Senjem, E. Dicks, N. Corriveau-Lecavalier, C. T. Mester, H. J. Wiste, E. S. Lundt, M. E. Murray, et al., Synthesizing images of tau pathology from cross-modal neuroimaging using deep learning, *Brain* 147 (3) (2024) 980–995.
- [65] D. C. Matthews, J. W. Kinney, A. Ritter, R. D. Andrews, E. N. Toledano Strom, A. S. Lukic, L. N. Koenig, C. Revta, H. M. Fillit, K. Zhong, et al., Relationships between plasma biomarkers, tau pet, fdg pet, and volumetric mri in mild to moderate alzheimer’s disease patients, *Alzheimer’s & Dementia: Translational Research & Clinical Interventions* 10 (3) (2024) e12490.